



HAL
open science

A mixed-dimensional CutFEM methodology for the simulation of fibre-reinforced composites

Pierre Kerfriden, Susanne Claus, Iulia Mihai

► **To cite this version:**

Pierre Kerfriden, Susanne Claus, Iulia Mihai. A mixed-dimensional CutFEM methodology for the simulation of fibre-reinforced composites. *Advanced Modeling and Simulation in Engineering Sciences*, In press. hal-02529651v1

HAL Id: hal-02529651

<https://hal.science/hal-02529651v1>

Submitted on 2 Apr 2020 (v1), last revised 4 May 2021 (v2)

HAL is a multi-disciplinary open access archive for the deposit and dissemination of scientific research documents, whether they are published or not. The documents may come from teaching and research institutions in France or abroad, or from public or private research centers.

L'archive ouverte pluridisciplinaire **HAL**, est destinée au dépôt et à la diffusion de documents scientifiques de niveau recherche, publiés ou non, émanant des établissements d'enseignement et de recherche français ou étrangers, des laboratoires publics ou privés.

A mixed-dimensional CutFEM methodology for the simulation of fibre-reinforced composites

P. Kerfriden^{1,2}, S. Claus³, I. Mihai²

¹ Centre des matériaux, Mines ParisTech, PSL University, France,
pierre.kerfriden@mines-paristech.fr

² School of Engineering, Cardiff University, United Kingdom,
mihailc1@cardiff.ac.uk

³ Onera Palaiseau, France,
susanne.claus@onera.fr

Abstract

We develop a novel unfitted finite element solver for composite materials with quasi-1D fibrous reinforcements. The method belongs to the class of mixed-dimensional non-conforming finite element solvers. The fibres are treated as 1D structural elements that may intersect the mesh of the embedding structure in an arbitrary manner. No meshing of the unidimensional elements is required. Instead, fibre solution fields are described using the trace of the background mesh. A regularised “cut” finite element formulation is carefully designed to ensure that analyses using such non-conforming finite element descriptions are stable. We also design a dedicated primal/dual operator splitting scheme to resolve the coupling between structure and fibrous reinforcements efficiently.

The novel computational strategy is applied to the solution of stiff computational models whereby fibrous reinforcements may lose their bond to the embedding material above a certain level of stress. It is shown that the primal-dual 1D/3D CutFEM scheme is convergent and well-behaved in variety of scenarios involving such highly nonlinear structural computations.

keywords: mixed-dimensional analysis, quasi-1D structural elements, CutFEM, nonconforming finite element method, LaTin solver, phase-field model, fibre-reinforced composite

Contents

1	Introduction	2
2	Embedded fibre problem	3
2.1	Elastic composite with perfectly bonded embedded fibres	4
2.2	Embedded elastic fibres with perfectly plastic bonding	5
3	Stabilised enriched finite element formulation	7
3.1	Time discretisation	7
3.2	Cut finite element formulation	7
3.3	Stabilisation	9
4	Operator-splitting LaTin algorithm	10
4.1	Overview	10
4.2	Linear stage: uncoupled systems of equations	11

4.3	“Inf-Sup-regularised” local stage: algorithmic solution	11
5	Numerical examples	11
5.1	2D structure with a hole and two embedded 1D reinforcements	11
5.2	Self-healing concrete block with temperature-activated elastic fibres	17
5.3	Fracture of quasi-brittle composites with randomly distributed short fibres	22
6	Conclusion	24
A	Unregularised LaTIn local stage	27

1 Introduction

In this paper, we develop an efficient unfitted finite element solver for composite materials and structures featuring fibrous reinforcements. Such composites are commonly used in industry. In civil engineering, standard concrete structures are reinforced with steel lattices to circumvent the poor ability of concrete to keep its integrity under tensile loading. Short fibres may be also be added to concrete mixes to increase their strength and ductility. To characterise and certify engineering structures employing such reinforced composites, it is important to devise efficient and reliable finite element solvers to simulate the associated micro-mechanics.

Simulations involving ”quasi-1D” embedded structural elements are difficult to carry in a standard finite element context. Indeed, representing such slender elements using finite elements that are dimensionality consistent with the embedding space leads to prohibitively large computational models. The 3D analysis of large-scale slender elements may at best be performed locally [23]. Away from regions of interest, asymptotic or numerical cross-sectional approximations of the mechanics of these structures need to be derived for numerical models to be tractable. In the context of quasi-1D embedded fibres, slender elements are typically represented as unidimensional structures with the properties of bars or beams. The mechanical coupling between these lower-dimensional elements and the surrounding domain needs to be handled with care when developing finite element solvers.

Following the taxonomy proposed in [23], three traditional finite element methodologies may be distinguished. In the diffuse approach (see e.g. [28]), stiffness is added to the element of the embedded domain that are intersected by reinforcements, leading to the desired local anisotropy. Such formulations are restricted to the analysis of arrays of slender elements that are geometrically regular and mechanically perfectly bonded to the surrounding material. In the discrete, conforming approach (see e.g. [28]), reinforcements are geometrically represented by edges of the embedding finite element mesh. The advantage is that slender elements may now possess their own kinematics, allowing to simulate sliding for example. However, elements of the embedding domain need to conform to the geometry of the fibrous reinforcement, leading to additional cost, and potentially to meshing difficulties. Finally, modern computational approach may use an embedded representation of fibres, whereby fibres are explicitly represented but may cross elements of the surrounding material in an arbitrary manner [17, 27, 23, 5]. The present methodology belongs to the latter class of methods.

We focus in this paper on the simulation of 2D and 3D structures reinforced by 1D unidimensional structural elements. The reinforcements will be straight and we will assume that they have no bending energy (i.e. bars in tension and compression). In this specific but important engineering context, we propose to develop a novel primal/dual CutFEM approach to model the assembly of composite components. The fibres will possess their own degrees of freedom, as in [15, 10]. This fundamental feature will be leveraged to represent sliding behaviours between the fibres and the surrounding material. Consistently with the CutFEM framework [18, 6], no specific computational mesh will be created to represent the 1D reinforcements. Instead unidimensional mechanical fields will be described as the trace of intersected embedded elements. Such formulations have already been explored to solve Laplace-Beltrami equations over embedded manifolds [10, 9], and to solve fluid flow problems in networks of cracks [14, 16, 10].

The novelty of the CutFEM approach proposed in the present paper is threefold. Firstly, we extend the "CutFEM on embedded manifolds" premise to the solution of advanced nonlinear solid mechanics problems involving unidimensional reinforcements. Secondly, we propose an efficient primal-dual numerical algorithm based on the LaTIn algorithm [22, 21, 3] to solve the 1D/3D coupled problem iteratively. This primal-dual formulation is a natural extension of our previous work on primal-dual CutFEM technologies for unilateral contact problems [12] (see [19, 26, 8, 1] for closely related pieces of work from other research groups), and is relatively new in the context of CutFEM approaches, where consistent penalty formulations are usually chosen as a first step to the development of a coupling strategy [7, 11, 13]. Finally, CutFEM formulations need to be carefully regularised for system matrices to be well conditioned and, in the context of primal-dual algorithms, for inf-sup stability conditions to be satisfied. The regularisation technique proposed in this paper departs from earlier work [10] in that it is devised specifically for primal-dual coupling conditions and that it relies on a consistent combination of ghost penalty regularisation [6] and added diffusion in the band of intersected embedding elements [10].

The proposed CutFEM methodology is to be applied to a family of nonlinear problems that are relevant to civil engineering design. We have two application targets in mind. Firstly, we wish to develop a solver for fracture in short-fibre reinforced concrete structures. Inclusions and inclusion/matrix nonlinear interface conditions will be handled efficiently using the primal-dual CutFEM algorithm presented in [11]. The proposed primal-dual algorithm will allow us to represent stiff slender reinforcements using a very similar algorithm, ensuring that the new developments proposed here are fully compatible with our existing computational library. Matrix failure will be represented by using the phase-field model and staggered solution algorithm presented in [25], without modification. Secondly, we wish to develop a methodology to simulate fibre pull-out. To this end, another novel element of the paper is the development of a new formulation for imperfectly bonded 1D fibres in 3D materials. More precisely, sliding will be allowed above a certain threshold, following a thermodynamically consistent approach, yielding a primal-dual stiff friction model (or a model of perfect plasticity with infinite stiffness for the 1D/3D interface) whose solution will be naturally handled by the LaTIn algorithm.

The article is organised as follows. In section 2, we present the problem setting. Straight elastic unidimensional fibres are embedded in a background elastic (potentially damageable) material. The new imperfect bonding formulation is presented next. In section 3, we present the primal-dual cut finite element formulation that will be dedicated to the solution of composite materials with fibrous reinforcements. Stabilisation aspects are carefully detailed in this section. The LaTIn iterative scheme is detailed in section 4. Finally, numerical results to demonstrate the efficiency and versatility of the proposed solver are reported and discussed in section 5.

2 Embedded fibre problem

We consider the problem of an elastic body occupying domain $\Omega \subset \mathbb{R}^d$ in dimension $d \in \{2, 3\}$. The material is reinforced by N_f straight unidimensional fibres. The i^{th} fibre occupies domain

$$\Gamma_f^i = \{x \in \Omega \mid x = P_1^i + \alpha(P_2^i - P_1^i), \alpha \in [0, 1]\}, \quad (1)$$

where P_1^i and P_2^i are two elements of \mathbb{R}^d . As a particular case, P_1^i and P_2^i are the extremities of fibre i if both points belong to domain Ω . We define $\Gamma_f = \bigcup_{i=1}^{N_f} \Gamma_f^i$ and we further assume that $\Gamma_f^i \cap \Gamma_f^j = \emptyset$ if $i \neq j$ (i.e. the fibres do not intersect). We define the director vector t_f^i of the i th fibre as $t_f^i = \frac{(P_2^i - P_1^i)}{\|P_2^i - P_1^i\|_2}$. The norm used is the euclidean norm. Here, t_f will denote the field defined over Γ_f whose value is t_f^i in Γ_f^i . We also introduce basis n_f (respectively (n_f^1, n_f^2)) for the line (respectively the plane) normal to t_f , in the case $d = 2$ (respectively $d = 3$). The boundary of domain Ω is denoted by $\partial\Omega$ and is additively split into a Dirichlet part $\partial\Omega_d$ and a Neumann part $\partial\Omega_n$.

We denote by $u_m : \Omega \rightarrow \mathbb{R}^d$ the displacement field of the matrix of the composite material. Here, u_m will be searched in Sobolov space $\mathcal{U}_m = \mathcal{H}^1(\Omega)$ of functions whose derivatives up to order one are

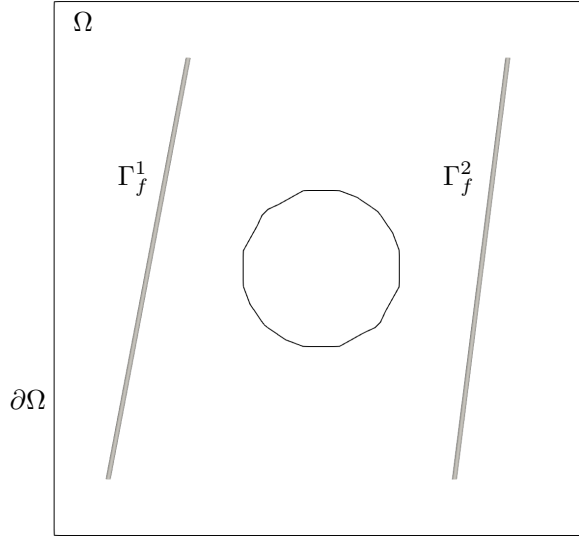


Figure 1: Computational domain with two embedded 1D fibres. The fibres have no bending energy.

square integrable. The displacement of the i^{th} fibre is denoted by $u_f^i : \Gamma_f^i \rightarrow \mathbb{R}^d$, and we additionally introduce notation $u_f : \Gamma_f \rightarrow \mathbb{R}^d$ to denote the field of Γ_f whose restriction to subdomain $\Gamma_f^i \subset \Gamma_f$ is u_f^i . We seek field u_f in product space $\mathcal{U}_f = \prod_{i=1}^{n_f} \mathcal{H}^1(\Gamma_f^i)$.

2.1 Elastic composite with perfectly bonded embedded fibres

To ease the reader into the proposed numerical scheme, we first introduce a simple solid mechanics problem whereby the matrix and fibres are linear elastic, and where the bonding between these two phases is perfect (i.e. there is no displacement jump). We therefore seek a solution $u := (u_m, u_f) \in \mathcal{U}_m \times \mathcal{U}_f$ minimising the energy functional

$$J(u_m, u_f) = E_m(u_m) + E_f(u_f), \quad (2)$$

where the potential energy functionals E_m and E_f are defined by

$$E_m(u_m) = \frac{1}{2} \int_{\Omega} \nabla_s u_m : C : \nabla_s u_m \, dx - \int_{\Omega} f_d \cdot u_m \, dx - \int_{\partial\Omega_n} t_d \cdot u_m \, dx \quad (3)$$

and

$$E_f(u_f) = \frac{1}{2} \sum_{i=1}^{n_f} \int_{\Gamma_f^i} k_f \nabla_f u_f : \nabla_f u_f \, dx, \quad (4)$$

respectively. In the previous expressions, $\nabla_s \cdot = \frac{1}{2} (\nabla \cdot + (\nabla \cdot)^T)$ is the symmetric part of the displacement gradient. ∇_f is the projected gradient operator defined as

$$\nabla_f \cdot = (t_f \otimes t_f) : \nabla \cdot \quad (5)$$

Field $f_d : \Omega \rightarrow \mathbb{R}^d$ is a volume source term, and $t_d : \partial\Omega_n \rightarrow \mathbb{R}^d$ is a field of Neumann conditions. Finally, $k_f \in \mathbb{R}$ is a fibre stiffness parameter, and $C \in (\mathbb{R}^d)^4$ is the fourth-order Hooke tensor defined by its action, which in the case of isotropic materials is

$$C : \nabla_s \cdot = \lambda \text{Trace}(\nabla_s \cdot) I_d + 2\mu \nabla_s \cdot \quad (6)$$

In the previous expression I_d is the identity tensor, and λ and μ are the Lamé constants. Importantly, due to the action of the projector gradient operator, the fibres have no bending energy.

The minimisation of J must be performed under constraints

$$u_m = u_d \quad \text{in } \partial\Omega_d \quad (7)$$

and

$$u_m - u_f = 0 \quad \text{in } \partial\Gamma_f. \quad (8)$$

The last equality enforces perfect bonding between matrix and elastic fibres.

The problem of minimisation under constraint can be recast as the unconstrained extremisation of a Lagrangian. The corresponding variational principle is the following Euler-Lagrange system of coupled equations: Find $(u_m, u_f, \lambda) \in \mathcal{U}_m \times \mathcal{U}_f \times \mathcal{Z}$ such that for all $(\delta u_m, \delta u_f, \delta \lambda) \in \mathcal{U}_m \times \mathcal{U}_f \times \mathcal{Z}$

$$\begin{aligned} \int_{\Omega} \nabla_s u_m : C : \nabla_s \delta u_m dx + \int_{\Gamma_f} k_f \nabla_f u_f : \nabla_f \delta u_f dx - \int_{\Gamma_f} \lambda \cdot (\delta u_m - \delta u_f) dx \\ = \int_{\Omega} f_d \cdot \delta u_m dx + \int_{\partial\Omega_n} t_d \cdot \delta u_m dx, \end{aligned} \quad (9)$$

and

$$\int_{\Gamma_f} \delta \lambda \cdot (u_m - u_f) dx = 0 \quad (10)$$

with the additional condition that Dirichlet condition (7) must be satisfied. We have used notation $\mathcal{Z} = \mathcal{L}^2(\Gamma_f)$. Here, the Lagrange multiplier field $\lambda \in \mathcal{Z}$ can be interpreted as the opposite of a density of forces applied by the embedding material to the 1D fibres (choose $\delta u_m = 0$ in (9) to see this).

For later use we define the jump operator by $[u] := u_m - u_f$, where we implicitly assume the existence of the cartesian product u between u_m and u_f .

2.2 Embedded elastic fibres with perfectly plastic bonding

We now relax perfect bonding condition (8) and only impose it in directions that are normal to the fibre directors, *i.e.*

$$\forall i \in \llbracket 1, d-1 \rrbracket, \quad [u] \cdot n_f^i = 0 \quad \text{in } \Gamma_f^i, \quad (11)$$

which may also be compactly written as

$$\Pi_f^\perp [u] = 0 \quad \text{in } \Gamma_f, \quad (12)$$

where $\Pi_f^\perp \cdot = (I_d - t_f \otimes t_f) \cdot$. For later use, we split λ as follows:

$$\lambda = \Pi_f \lambda + \Pi_f^\perp \lambda := (I_d - \Pi_f^\perp) \lambda + \Pi_f^\perp \lambda = (t_f \otimes t_f) \lambda + \Pi_f^\perp \lambda =: \lambda_f^\Pi t_f + \Pi_f^\perp \lambda, \quad (13)$$

We assume that equilibrium equation (9) is satisfied. Due to the relaxation of the bonding conditions, λ_f^Π is now undetermined. In the following, we introduce a rate-independent plasticity-like evolution law for this quantity, following the classical framework of thermodynamically consistent materials.

The nonlinear time analysis will be conducted over pseudo-time interval $\mathcal{T} = [0, T]$. Field u_m, u_f and λ are now defined over product spaces $\mathcal{U}_m \times \mathcal{T}$, $\mathcal{U}_f \times \mathcal{T}$ and $\mathcal{Z} \times \mathcal{T}$, respectively. For the sake of simplicity, the initial conditions $u_m(\cdot, 0)$ and $u_f(\cdot, 0)$ will be set to zero.

At any time $t \in \mathcal{T} \setminus \{0\}$, the energy dissipation is defined by

$$\mathcal{D}(u_m, u_f, \lambda) = \mathcal{P}_e(u_m, u_f) - \frac{d}{dt} (\psi(u_m, u_f)), \quad (14)$$

where the power of the external forces is

$$\mathcal{P}_e(u_m, u_f) = \left(\int_{\Omega} f_d \cdot \dot{u}_m \, dx + \int_{\partial\Omega_n} t_d \cdot \dot{u}_m \, dx \right) \quad (15)$$

and the elastic energy of the composite is defined as

$$\psi(u_m, u_f) = \frac{1}{2} \left(\int_{\Omega} \nabla_s u_m : C : \nabla_s u_m \, dx + \int_{\Gamma_f} k_f \nabla_f u_f : \nabla_f u_f \, dx \right). \quad (16)$$

Replacing the test functions by velocities in (9), the energy dissipation takes the following expression:

$$\mathcal{D}(u_m, u_f, \lambda) = \int_{\Gamma_f} \lambda^{\Pi} \cdot [\dot{u}]^{\Pi} \, dx \quad (17)$$

where $\lambda^{\Pi} := t_f \cdot \lambda$.

We now postulate that solution (u_m, u_f, λ) satisfies the principle of maximum energy dissipation at all times, subject to the following inequality constraint:

$$f_f(\lambda^{\Pi}) := |\lambda^{\Pi}| - Y \leq 0 \quad \text{in } \Gamma_f, \quad (18)$$

where Y is the unique positive scalar parameter of the friction model. The constrained maximisation principle will yield an expression for the evolution of λ^{Π} , which is ensured by the convexity of f_f . Introducing and extremising Lagrangian

$$\mathcal{L}_f^{\Pi}(\lambda^{\Pi}, \gamma_f) := \mathcal{D}(u_m, u_f, \lambda^{\Pi}) + \int_{\Gamma_f} \gamma_f f_f(\lambda^{\Pi}) \, dx \quad (19)$$

with respect to λ^{Π} and Lagrange multiplier γ_f , we obtain the usual Karush-Kuhn-Tucker conditions, which are composed of the three relations

$$f_f(\lambda^{\Pi}) \leq 0 \quad \gamma_f f_f(\lambda^{\Pi}) = 0 \quad \gamma_f \geq 0 \quad (20)$$

and of variational equality

$$\forall \delta \lambda^{\Pi} \in \mathcal{L}^2(\Gamma_f), \quad \mathcal{D}(u_m, u_f, \delta \lambda) + \int_{\Gamma_f} \gamma_f f'_f(\lambda^{\Pi})(\delta \lambda \cdot t_f) \, dx = 0, \quad (21)$$

where $f'_f(\cdot) = \text{sign}(\cdot)$. The last equation yields the following expression for the Lagrange multiplier:

$$\gamma_f = -\text{sign}(\lambda^{\Pi}) [\dot{u}]^{\Pi}. \quad (22)$$

We can finally state the system of equations that governs the evolution of the composite with imperfectly bonded fibres. The system is composed of equilibrium equation (9) perfect normal bonding equation (11) and the system of equations for the plastic flow of the fibre/matrix bond in the direction of the fibre director vectors

$$f_f(\lambda^{\Pi}) \leq 0 \quad f_f(\lambda^{\Pi}) [\dot{u}]^{\Pi} = 0 \quad \text{sign}(\lambda^{\Pi}) [\dot{u}]^{\Pi} \leq 0. \quad (23)$$

The last inequality implies, in particular, that the dissipation is always positive, which means that the proposed model satisfies the second principle of thermodynamics. Whilst the two first equations allow us to calculate the amplitude of λ^{Π} , the last one yields its sign. It is clear that λ^{Π} acts in opposition to the motion of the matrix relative to the fibres.

3 Stabilised enriched finite element formulation

3.1 Time discretisation

We use the implicit Euler scheme to discretise the time derivatives that appear in the plasticity model. \mathcal{T} is split into n_t time slabs of equal length ΔT . The resulting discrete time grid is denoted by $\mathcal{T}_{\Delta t} = \{t_0, t_1, \dots, t_{n_t}\}$. At time t_n , $n > 0$, system (23) becomes:

$$\begin{cases} f_f(\lambda^\Pi(t_n)) \leq 0 \\ f_f(\lambda^\Pi(t_n)) ([u(t_n)]^\Pi - [u(t_{n-1})]^\Pi) = 0 \\ \text{sign}(\lambda^\Pi(t_n)) ([u(t_n)]^\Pi - [u(t_{n-1})]^\Pi) \leq 0. \end{cases} \quad (24)$$

Notice that step length ΔT does not appear in this set of rate-independent equations (*i.e.* pseudo-time dependency).

3.2 Cut finite element formulation

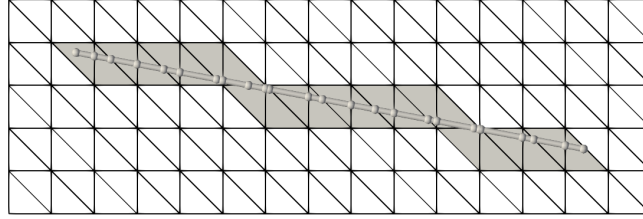


Figure 2: Primal and dual fibre fields are represented by the trace of bulk finite element spaces.

Finite element spaces. We will solve the composite problem using an enriched finite element formulation. In particular, the embedded fibres will possess their own degrees of freedom defined via the finite element space of the embedding material restricted to the band of intersected elements.

Let us introduce a triangulation \mathcal{T}_h of domain Ω . Here, h is the diameter of the smallest sphere containing the elements of \mathcal{T}_h . We now define the finite element space $\mathcal{U}_h \subset \mathcal{U}_m$ by

$$\mathcal{U}_h := \{u \in \mathcal{C}^0(\Omega) \mid u|_K \in \mathcal{P}^1(K) \forall K \in \mathcal{T}_h\}. \quad (25)$$

Next, we define the set of all elements of \mathcal{T}_h that have a non-zero intersection with Γ_f (*i.e.* grey elements in Figure 2) by

$$\mathcal{G}_h := \{K \in \mathcal{T}_h \mid K \cap \Gamma_f \neq \emptyset\}. \quad (26)$$

The domain corresponding to this set is denoted by $G_h := \bigcup_{K \in \mathcal{G}_h} K$. Importantly, all fields defined over the embedded fibres will be represented by the restriction of finite element fields defined over G_h . We define the extended (in the sense extended from 1D embedded domain to the surrounding surface or volume) fibre finite element space \mathcal{W}_h by

$$\mathcal{W}_h := \{u \in \mathcal{C}^0(G_h) \mid u|_K \in \mathcal{P}^1(K) \forall K \in \mathcal{G}_h\}. \quad (27)$$

Of key importance to CutFEM methods [18, 7, 12] is the introduction of regularisation terms to ensure that system matrices remain well-conditioned, notably by applying some form of ghost-penalty [6] stabilisation. To this end, we define the set of intersected element edges by

$$\mathcal{F}_I := \{F = K \cap K' \mid K \in \mathcal{G}_h \text{ and } K' \in \mathcal{G}_h\}. \quad (28)$$

Finite element formulation. At time t_n , $n > 0$, we look for a solution composed of fields $u_h := (u_{m,h}, u_{f,h}, \lambda_h, \tilde{w}_h, \tilde{\lambda}_h) \in \mathcal{U}_h \times \mathcal{W}_h \times \mathcal{W}_h \times \mathcal{Z} \times \mathcal{Z}$. Here, $u_{m,h}$ is the finite element displacement in the matrix phase. $u_{f,h}$ is a finite element field defined over the band of elements intersected by the fibers, and whose restriction to the 1D fiber domains will be our finite element approximation of the fiber displacements. λ_h is the extended approximation of the Lagrange multiplier field, which will be sought for in the same space as $u_{f,h}$. Fields \tilde{w}_h and $\tilde{\lambda}_h$ are additional variables that need to be introduced to stabilise the CutFEM formulation. $\tilde{\lambda}_h$ is a fiber Lagrange multiplier field that belongs in $\mathcal{L}^2(\Gamma_f)$. Finally, \tilde{w}_h is a field that represents the jump of displacement between the fibers and the surrounding matrix material. This field will also be looked for in $\mathcal{L}^2(\Gamma_f)$. Fields \tilde{w}_h and $\tilde{\lambda}_h$ are not discretised *a priori*. Their numerical values will only be required at quadrature points defined over interface Γ_f (through the discrete evaluation of integrals). The 5 fields introduced here are fully defined by the set of equations provided below.

To avoid cluttered symbolic expressions, we will omit the dependency of solution fields to time. The only exception is for quantities at time t_{n-1} , which will be indicated via the $*$ superscript. Other notations, notably the use of superscript Π and jump symbol $[\cdot]$ are meant to be consistent with the developments of the previous sections, and should be self-explanatory.

The enriched finite element formulation of the embedded fibre problem employs a two-scale formalism that requires splitting \mathcal{Z} additively into the restriction of \mathcal{W}_h onto Γ_f and its supplementary space. Accordingly, the stabilised and extended \mathcal{L}^2 -projection $\lambda_h \in \mathcal{W}_h$ of field $\tilde{\lambda}_h \in \mathcal{Z}$ is defined by

$$\forall \delta \lambda_h \in \mathcal{W}_h, \quad (\lambda_h - \tilde{\lambda}_h, \delta \lambda_h)_{\mathcal{L}^2(\Gamma_f)} + s_{\heartsuit,h}(\lambda_h, \delta \lambda_h) = 0. \quad (29)$$

Here, term $s_{\heartsuit,h}$ is a regularisation term that will be discussed in the next section.

Now, solution $(u_{m,h}, u_{f,h}, \lambda_h, \tilde{w}_h, \tilde{\lambda}_h)$ must satisfy the previous identity, the Dirichlet conditions for $u_{m,h}$ and the following variational statement For all $(\delta u_{m,h}, \delta u_{f,h}) \in \mathcal{U}_h \times \mathcal{W}_h$, and providing that $\delta u_{m,h}$ satisfies the homogeneous Dirichlet boundary conditions,

$$a_h((u_{m,h}, u_{f,h}), (\delta u_{m,h}, \delta u_{f,h})) - (\lambda_h, [\delta u_h])_{\mathcal{L}^2(\Gamma_f)} = l_h((\delta u_{m,h}, \delta u_{f,h})). \quad (30)$$

This variational equality is complemented by the Signorini-type law for the $\tilde{\cdot}$ quantities

$$\text{locally in } \Gamma_f, \quad \begin{cases} f_f(\tilde{\lambda}_h^\Pi) \leq 0 \\ f_f(\tilde{\lambda}_h^\Pi) \cdot (\tilde{w}_h^\Pi - \tilde{w}_h^{*\Pi}) = 0 \\ \text{sign}(\tilde{\lambda}_h^\Pi) (\tilde{w}_h^\Pi - \tilde{w}_h^{*\Pi}) \leq 0, \end{cases} \quad (31)$$

and by $d - 1$ scalar equality constraints

$$\text{locally in } \Gamma_f, \quad \Pi_f^\perp \tilde{w}_h = 0. \quad (32)$$

Last, the following closure equation is introduced, following [12]

$$(\lambda_h - \tilde{\lambda}_h) - \gamma([u_h] - \tilde{w}_h) = 0. \quad (33)$$

The last equation regularises the $\tilde{\cdot}$ interface quantities by penalising the distance to their ${}_h$ bulk counterpart. Parameter γ must be strictly positive. The bilinear and linear forms used in (30) are respectively defined by

$$\begin{aligned} a_h((u_{m,h}, u_{f,h}), (\delta u_{m,h}, \delta u_{f,h})) &= \int_{\Omega} \nabla_s u_{m,h} : C : \nabla_s \delta u_{m,h} \, dx \\ &+ \int_{\Gamma_f} k_f \nabla_f u_{f,h} : \nabla_f \delta u_{f,h} \, dx \\ &+ s_{\sharp,h}(u_{f,h}, \delta u_{f,h}) \end{aligned} \quad (34)$$

and

$$l_h((\delta u_{m,h}, \delta u_{f,h})) = \int_{\Omega} f_d \cdot \delta u_{m,h} \, dx + \int_{\partial\Omega_n} t_d \cdot \delta u_{m,h}. \quad (35)$$

Here, term $s_{\sharp,h}$ is the second regularisation term of the formulation. It is discussed next.

3.3 Stabilisation

Without stabilisation (*i.e.* definition of $s_{\sharp,h}$, $s_{\heartsuit,h}$ and mixed condition (33)), the 1D-3D CutFEM formulation suffers from several sources of numerical instability.

1. Elements may have a small intersection with a particular fibre, leading to a loss of control of finite element field $u_{f,h}$ (fibre displacement, which is extended to the band of intersected elements) and finite element field $\lambda_{f,h}$.
2. The extended fibre kinematics (displacements and Lagrange multipliers) allows zero energy modes to be represented, leading to singular systems of equations.
3. Uncontrolled oscillatory modes may appear in the Lagrange multiplier fields due to the non-satisfaction of the LBB condition.

These problems will be circumvented via the introduction of the following regularisation term:

$$\begin{aligned} s_{\sharp,h}(u_{f,h}, \delta u_{f,h}) &= \beta k_f h^{2-d} \sum_{F \in \mathcal{F}_I} \int_F ([\nabla_f u_{f,h}] \cdot n_F) ([\nabla_f \delta u_{f,h}] \cdot n_F) dx \\ &+ \zeta k_f h^{1-d} \int_{G_h} \nabla_f^\perp u_{f,h} : \nabla_f^\perp \delta u_{f,h} dx, \end{aligned} \quad (36)$$

where n_F denotes the facet normal and the orthogonal gradient operator is defined by

$$\nabla_f^\perp u_{f,h} = \nabla u_{f,h} - \sum_{i=1}^d (\nabla(u_{f,h} \cdot e_i) \cdot t_f) e_i \otimes t_f. \quad (37)$$

Ghost penalty parameter β is typically set to 0.1. The corresponding term extends the ellipticity provided by the fibres' elasticity operator to the entire band of intersected elements, thereby alleviating the ill-conditioning due to uncontrolled modes of $u_{f,h} \cdot t_f$. Let us emphasise that only the tangential part of $u_{f,h}$ is controlled by the ghost-penalty stabilisation. This is consistent with the formulation of the deformation energy of the fibres, which develops in reaction to the projected displacement gradient. The normal part of the fibre displacement does not need to be regularised. It will simply follow the bulk displacement, which is trivially enforceable, the fibre having no bending energy to act against the corresponding constraint. This addresses point 1 above.

The second regularisation term eliminates zero energy modes from the system, which addresses point 2 above. It is a diffusion term which is integrated over the entire band of element, although a facet penalisation could have been used as well [10]. This term does not introduce any inconsistency (an extension of the exact solution in the normal direction may be constructed, which has vanishing orthogonal gradient). Typically, a small parameter value $\zeta = 10^{-5}$ is sufficient to stabilise the formulation.

A similar term is proposed to stabilise the Lagrange multiplier field (see Points 1 and 3 above):

$$\begin{aligned} s_{\heartsuit,h}(\lambda_h, \delta \lambda_h) &= \beta_\lambda \frac{1}{\kappa} h^{6-d} \sum_{F \in \mathcal{F}_I} \int_F ([\nabla_f \lambda_h] \cdot n_F) ([\nabla_f \delta \lambda_h] \cdot n_F) dx \\ &+ \zeta_\lambda \frac{1}{\kappa} h^{5-d} \int_{G_h} \nabla_f^\perp \lambda_h : \nabla_f^\perp \delta \lambda_h dx, \end{aligned} \quad (38)$$

where $\kappa = \frac{EL^{d-1}k_f}{EL^{d-1}+k_f}$ is the harmonic mean of the fibre stiffness and the equivalent axial stiffness provided by the matrix. L is a non-dimensionalising parameter that represents the width of the matrix region that reacts to the deformations of a particular fibre. As shown in [12], the first term helps control the spurious oscillations that may appear in the Lagrange multiplier field. The second term eliminates zero energy modes.

We showed in [12] that this type of stabilised primal/dual formulation could be interpreted as an alternative formulation for the stabilised augmented Lagrangian proposed in [8], in the spirit of the classical approach for unilateral contact problems first introduced in [2].

4 Operator-splitting LaTIn algorithm

4.1 Overview

We will develop a LaTIn solver that algorithmically decouples the matrix and fibre finite element problems. LaTIn solvers have proved to be particularly efficient when solving stiff Signorini-type problems without the need to further smoothen or regularise the discrete system of governing equations.

The primal/dual variables of interest are $F_h = (F_{m,h}, F_{f,h}) \in \mathcal{W}_h \times \mathcal{W}_h$, which represents $F_{m,h} \equiv \lambda_h$ and $F_{f,h} \equiv -\lambda_h$, and $W_h = (W_{m,h}, W_{f,h}) \in \mathcal{W}_h \times \mathcal{W}_h$ that represents the restriction of $u_{m,h}$ to the band of intersected elements G_h . One iteration of the LaTIn solver is as follows.

Linear stage. Knowing half-iterate $S^{k-\frac{1}{2}} := (W_h^{k-\frac{1}{2}}, F_h^{k-\frac{1}{2}})$, we look for $S^k := (W_h^k, F_h^k)$ satisfying differential equation (30), where

$$\text{in } G_h, \quad W_h^k = u_{m,h}^k. \quad (39)$$

To close the system of equations, we require the iterate to satisfy the descent search direction given by

$$\begin{cases} \left(F_{m,h}^k - F_{m,h}^{k-\frac{1}{2}} \right) + \gamma \left(W_{m,h}^k - W_{m,h}^{k-\frac{1}{2}} \right) = 0 \\ \left(F_{f,h}^k - F_{f,h}^{k-\frac{1}{2}} \right) + \gamma \left(W_{f,h}^k - W_{f,h}^{k-\frac{1}{2}} \right) = 0. \end{cases} \quad (40)$$

The differential equations of the matrix and fibres are decoupled by this algorithmic construction. Positive scalar γ was first introduced in equation (33). It is such that $\gamma = \bar{\gamma}\kappa L^{-1}$, where $\bar{\gamma}$ is a non-dimensional parameter.

Relaxation stage.

$$S^k \leftarrow \mu S^k + (1 - \mu) S^{k-1} \quad (41)$$

Relaxation parameter μ is typically set to 0.85 (see e.g. [3]).

Local stage. Knowing $S^k := (W_h^k, F_h^k)$, we look for $S^{k+\frac{1}{2}} := (W_h^{k+\frac{1}{2}}, F_h^{k+\frac{1}{2}})$ satisfying the set of requirements (29), (31), (32), (33), where we will introduce variables $\tilde{W}_h^{k+\frac{1}{2}} = (\tilde{W}_{m,h}^{k+\frac{1}{2}}, \tilde{W}_{f,h}^{k+\frac{1}{2}}) \in \mathcal{Z}^2$ and $\tilde{F}_h^{k+\frac{1}{2}} = (\tilde{F}_{m,h}^{k+\frac{1}{2}}, \tilde{F}_{f,h}^{k+\frac{1}{2}}) \in \mathcal{Z}^2$ and replace all occurrences of symbol u_h by symbol W_h , and λ_h by $F_{m,h}$. We further require that

$$\text{in } G_h, \quad F_{m,h}^{k+\frac{1}{2}} + F_{f,h}^{k+\frac{1}{2}} = 0 \quad (42)$$

and that (29) applies to both $F_{m,h}^{k+\frac{1}{2}}$ and $F_{f,h}^{k+\frac{1}{2}}$. To close the system of equations, we require the half-iterate iterate to satisfy the ascent direction

$$\begin{cases} \left(F_{m,h}^{k+\frac{1}{2}} - F_{m,h}^k \right) - \gamma \left(W_{m,h}^{k+\frac{1}{2}} - W_{m,h}^k \right) = 0 \\ \left(F_{f,h}^{k+\frac{1}{2}} - F_{f,h}^k \right) - \gamma \left(W_{f,h}^{k+\frac{1}{2}} - W_{f,h}^k \right) = 0. \end{cases} \quad (43)$$

Notice that because of closure equation (33) and extended projection property (29), the ascent search direction and equation (42) are also satisfied by the $\tilde{\cdot}^{k+\frac{1}{2}}$ quantities.

4.2 Linear stage: uncoupled systems of equations

The linear stage defined above consists in solving the following set of linear equations, which are independent for each phase of the composite:

$$\begin{aligned} \forall \delta u_{m,h} \in \mathcal{U}_h, \quad & \int_{\Omega} \nabla_s u_{m,h}^k : C : \nabla_s \delta u_{m,h} dx + \int_{\Gamma_f} \gamma u_{m,h}^k \cdot \delta u_{m,h} dx \\ & = l(\delta u_{m,h}) + \int_{\Gamma_f} \left(F_{m,h}^{k-\frac{1}{2}} + \gamma W_{m,h}^{k-\frac{1}{2}} \right) \cdot \delta u_{m,h} dx \end{aligned} \quad (44)$$

$$\begin{aligned} \forall \delta u_{f,h} \in \mathcal{W}_h, \quad & \int_{\Gamma_f} k_f \nabla_f u_{f,h}^k : \nabla_f \delta u_{f,h} dx + \int_{\Gamma_f} \gamma u_{f,h}^k \cdot \delta u_{f,h} dx + s_{\#,h}(u_{f,h}^k, \delta u_{f,h}) \\ & = \int_{\Gamma_f} \left(F_{f,h}^{k-\frac{1}{2}} + \gamma W_{f,h}^{k-\frac{1}{2}} \right) \cdot \delta u_{f,h} dx. \end{aligned} \quad (45)$$

As detailed previously, the set of equations corresponding to the fibres are regularised by term $s_{\#,h}$.

4.3 “Inf-Sup-regularised” local stage: algorithmic solution

The regularised local stage defined previously can be solved by applying the following algorithmic procedure.

- Choose an appropriate quadrature strategy for $\left(\tilde{F}_{m,h}, \delta F_{m,h} \right)_{\mathcal{L}^2(\Gamma_f)}$, where $\tilde{F}_{m,h} \in \mathcal{Z}$ and $\delta F_{m,h} \in \mathcal{W}_h$. At every integration point of set $\tilde{\mathcal{I}}_{f,h}$, solve nonlinear but local equations (31), (32), (42), (43) for $\tilde{F}_{m,h}^{k+\frac{1}{2}}$, knowing (W_h^k, F_h^k) . These calculations are classical when applying LaTIn solvers, and are fully detailed for the friction model introduced in this paper in appendix A.

- Solve extended and stabilised projection problem

$$\forall \delta F_{m,h} \in \mathcal{W}_h, \quad \left(F_{m,h}^{k+\frac{1}{2}}, \delta F_{m,h} \right)_{\mathcal{L}^2(\Gamma_f)} + s_{\heartsuit} \left(F_{m,h}^{k+\frac{1}{2}}, \delta F_{m,h} \right) = \left(\tilde{F}_{m,h}^{k+\frac{1}{2}}, \delta F_{m,h} \right)_{\mathcal{L}^2(\Gamma_f)}. \quad (46)$$

- Set $F_{f,h}^{k+\frac{1}{2}} = -F_{m,h}^{k+\frac{1}{2}}$ and recover $W_h^{k+\frac{1}{2}}$ by using ascent search direction (43).

In our example, we use the quadrature point corresponding to the integral of the product of two piecewise linear fields over Γ_f . This introduces a quadrature error, whose effect was studied and discussed in [12].

5 Numerical examples

All the numerical simulations presented in this section are performed using the LaTIn-CutFEM library [12] developed in finite element package FEniCS [4].

5.1 2D structure with a hole and two embedded 1D reinforcements

The first numerical example that we wish to discuss is represented in Figure 3. The structure is two-dimensional, and undergoes plane strain deformations. The computational domain is the unit square $\Omega = [0,1] \times [0,1]$. A vertical load is applied in the form of a Dirichlet field u_d at the top of the structure, i.e. $\partial\Omega_d = \{x \in \Omega \mid x \cdot e_2 = 1\}$. The Young’s modulus E in the circle of diameter $r = 0.15$ with centre $(0.5, 0.5)$ is set to 1.0. Outside the circle, the Young’s modulus is set to 0.1. Hence, the circular inclusion is made of a comparatively hard material. Poisson’s ratio for both materials are set to 0.3.

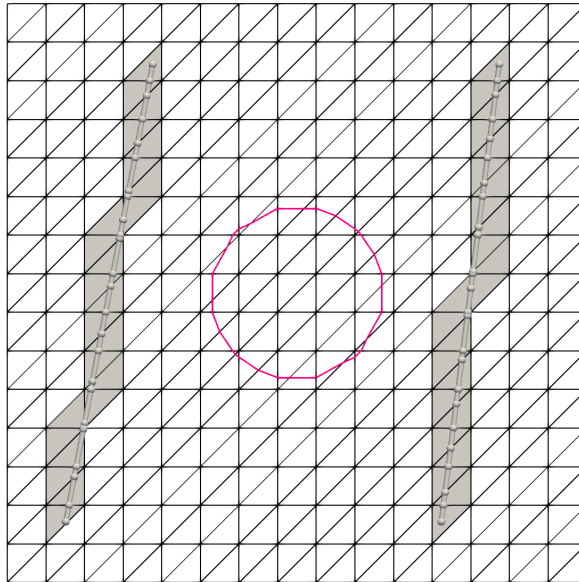


Figure 3: 2D example with an unfitted stiff circular inclusion and two 1D reinforcements.

Two straight reinforcements are introduced, as represented in Figure 3. The reinforcements are stiff compared to the matrix, with $k_f = 1.0$. The friction coefficient Y is relatively low at $Y = 0.2$, which will result in early yielding.

The prescribed displacement field is uniform over $\partial\Omega_d$, and of amplitude $A(t)$ as reported in Figure 5 (top subfigure). The structure is loaded in traction, then unloaded and forced into a compressive state, before being reloaded in traction. Figure 5 also shows the 26 time steps that will be used by the implicit time integrator. There is no source term, i.e. $f_d = 0$ and no imposed tractions, i.e. $t_d = 0$.

A coarse computational mesh is represented in Figure 3. The set of intersected cells \mathcal{G}_h over which the finite element fibre displacements and Lagrange multipliers are defined are also represented. The fibres do not conform with the regular background mesh. The circle does not conform to mesh edges either. In order to handle the mismatch in material properties, kinematic enrichment is performed using the CutFEM technology, including ghost penalty stabilisation and the primal/dual coupling introduced in [12].

We now examine Figure 4. The figure presents the field of Lagrange multipliers after the third time step (framed in the top subfigure of Figure 5). The colour scale indicates the magnitude of the Lagrange multipliers, which are piecewise linear in the band of intersected elements. We emphasise the fact that all our fibre fields are traces of d -dimensional standard finite element fields defined over these bands of intersected elements. Fibres do not possess their own meshes. We see that the multipliers are aligned with the director vectors. This is normal, but not enforced directly in our approach. Fibres do not have bending energy. Therefore, they can only generate forces in the direction of their respective director vector, thereby resisting to deformations of the matrix phase in these directions only. In our experience, erroneous stabilisation of the fibre fields generate tangential forces that pollute the overall finite element results.

In Figure 5, we report the evolution of these forces with time. Towards the end of the increasing phase of the loading amplitude $A(t)$, these forces saturate. Indeed, they are constrained not to exceed friction coefficient Y . Instead, plastic slip develops to accommodate the boundary conditions. At the end of the compression phase, the forces are also fully saturated, but take the opposite signs, as they now react to compressive loading. The last picture is interesting. It is representative of transition phases that appear when the direction of the load changes. In that case, forces at the extremities of the fibres immediately change directions, while due to adhesion, the forces in the middle of the fibres

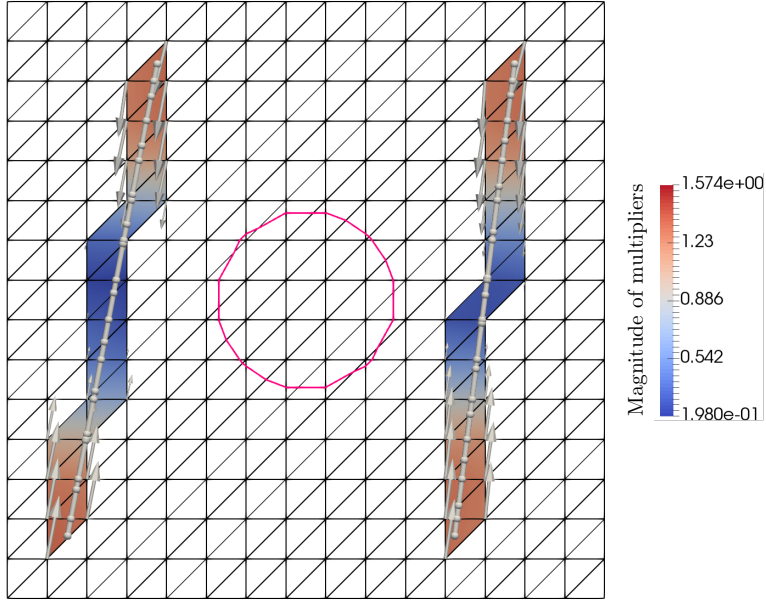


Figure 4: Forces applied by the fibers to the embedding material in reaction to an overall prescribed extension of the structure.

carry residual forces in the opposite direction, creating a mixed traction/compression stress state in the matrix as well. Notice that the degrees of freedom corresponding to the Lagrange multipliers are well-behaved throughout this analysis.

A sequence of computational meshes is represented in Figure 6. The solution is for the 20th of the computational times shown in Figure 5. The structure is globally in tension, but residual compressive stresses exist in the matrix due to the past global compression states. Looking at the finest of the finite element solutions, we see that stress concentrations develop at the extremities of the fibers. Away from these extremities, the stiff fibres restrict the value of the tensile stress that develops in the embedding material. It is clear that the stress field shown in Figure 6 converges with mesh refinement.

In Figure 7, the four meshes are warped using the displacement of the matrix phase, and both fibres are warped with their own displacement fields. The solution inside the circle is not represented. The absence of noticeable difference between the 4 displacement fields indicates that the method converges with mesh refinement. The symmetries observed in the displacement of the fibres are also qualitative indicators that the proposed strategy and its numerical implementation are correct. Notice that meshes now appear to conform to the geometry of the circular inclusion. These are not computational meshes but auxiliary meshes obtained by subdividing elements that are cut by the inner circle, which is done for integration and visualisation purposes only. The finite element meshes used to describe the displacement field in the matrix are the regular grids displayed in Figure 6.

In Figure 8, we present quantitative mesh convergence results for the example described above. We report the evolution of the reaction force at the Dirichlet boundary

$$R_h(t) = \int_{\partial\Omega_d} e_2 \cdot (C : \nabla_s u_{m,h}(t)) \cdot n \, dx \quad (47)$$

as a function of the loading amplitude. In the previous expression, $n = e_2$ is the outer normal to the Dirichlet domain boundary, and e_2 is the second canonical vector of \mathbb{R}^2 . Time response $R_h(t)$ is computed four times using the sequence of meshes represented in Figure 7. Clearly, the nonlinear behaviour of the interface between fibres and matrix creates an hysteresis that is akin to that of plastic materials undergoing cycling deformations. The area bounded by the upper and lower part of the cycle

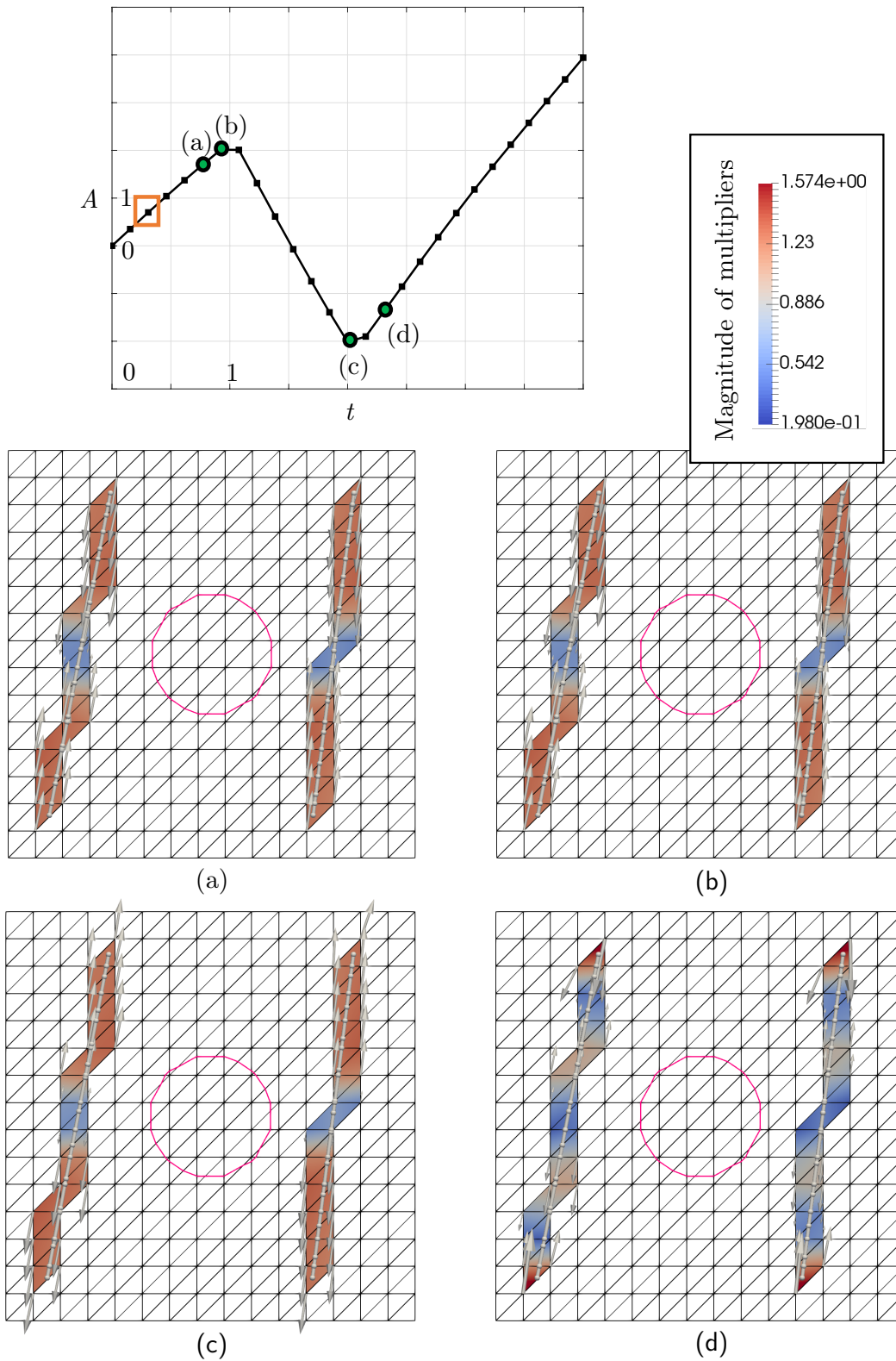


Figure 5: History of fiber reaction forces. Nonlinear effects are due to the friction law that governs possible sliding between the fibres and the embedding material. The amplitude of the forces is bounded by parameter Y of the adhesion/friction model.

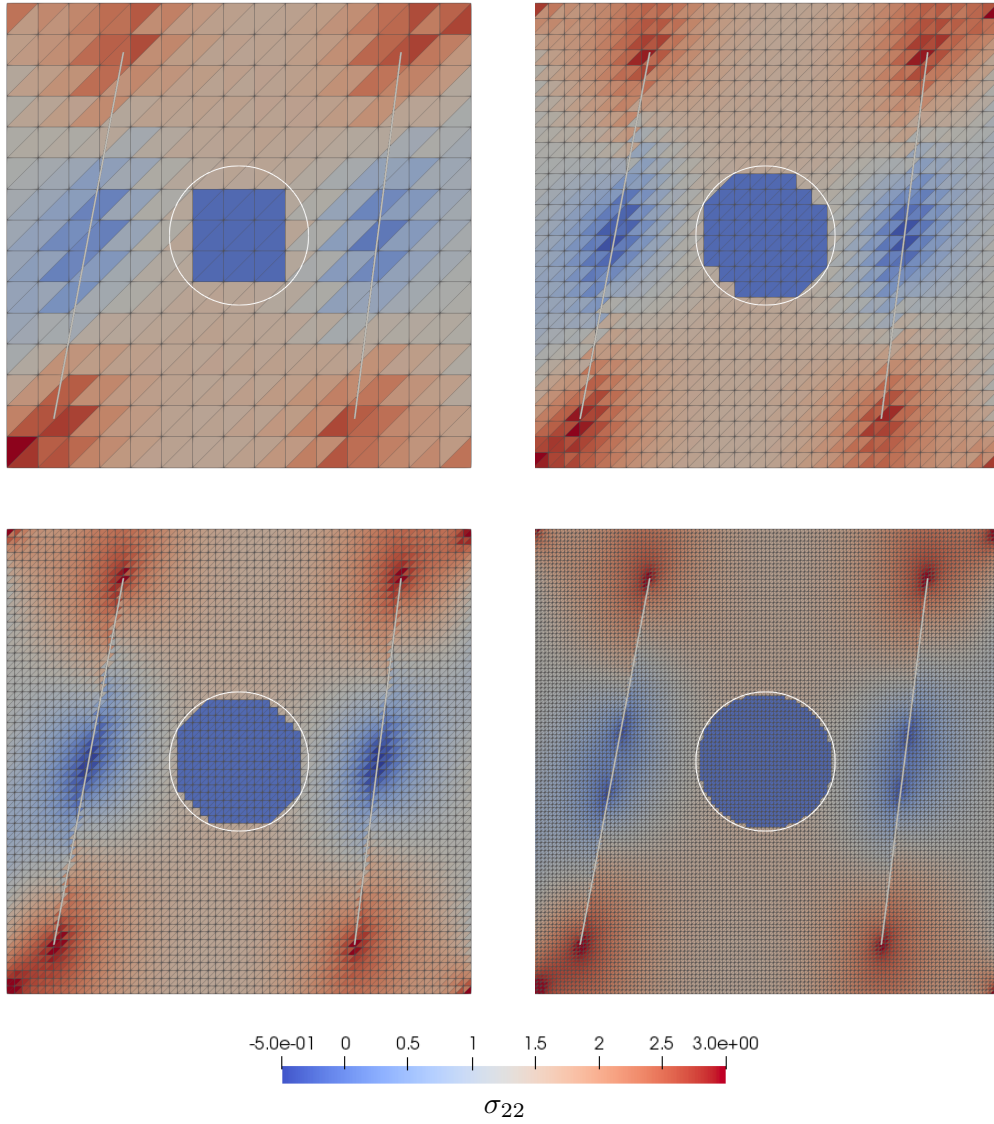


Figure 6: Normal component of the stress field in the vertical direction. The finite element solution is computed using 4 computational meshes.

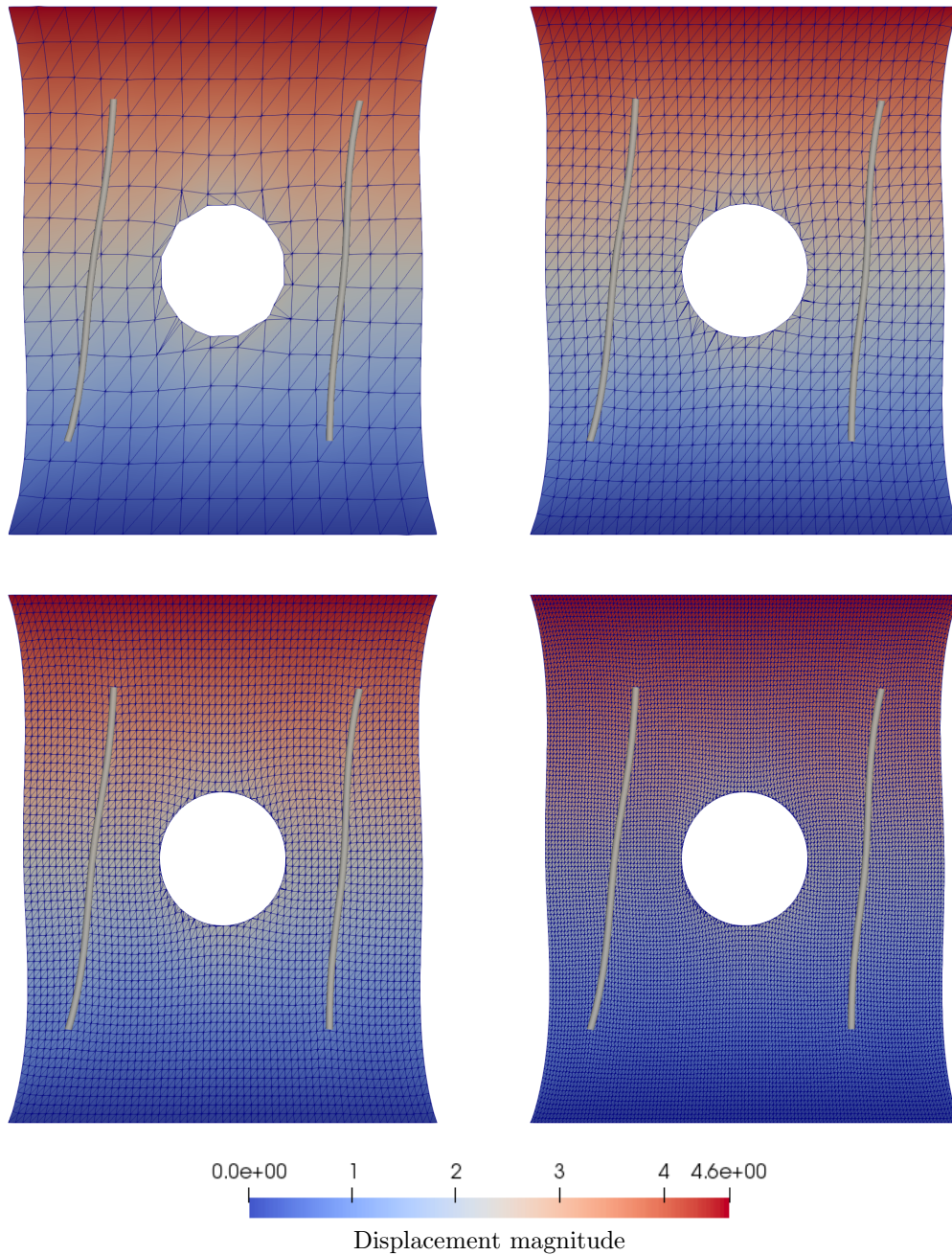


Figure 7: Warping of the computational domain and both 1D fibre domains by the corresponding displacement fields.

is the energy that has been dissipated during the cycle by friction. The response curve converges with mesh refinement.

5.2 Self-healing concrete block with temperature-activated elastic fibres

Description of the computational model. One of the motivating elements for the present work is the simulation of advanced concrete structures. In recent years, considerable work has been carried out in the development of self-healing cementitious materials. A particular application, currently investigated at Cardiff University, is the use of shrinkable fibres in the development of a crack closure system (see Figure 9). The fibres are made of polyethylene terephthalate (PET), a shape memory polymer (SMP) that shrinks when heated at temperatures above 60 Celsius [20]. Under restrained conditions and upon thermal activation these SMP fibres can develop significant shrinkage stresses [20, 24]. Preliminary results from an experimental study showed that SMP fibres with end-anchorages and embedded in a cementitious matrix were effective in closing macro-cracks [24]. Nevertheless, to achieve an optimum mix design for these advanced cement based composites, further work focused on the optimisation of key parameters (e.g. fibre geometry, fibre content) is required. To this end, virtual experiments carried out with numerical models that are able to capture the underlying mechanisms would be very advantageous.

We now propose to show how experimental devices such as the one represent in Figure 9 may be simulated using the proposed embedded FE technology, which we hope will eventually enable experimentalists to explore material design spaces virtually. The computational model is represented in Figure 10. It is composed of one main square parallelepiped (the beam), and four additional smaller square parallelepiped designed to replicate the loading conditions of typical testing devices used in civil engineering. We apply zero Dirichlet conditions along a line of each of the two smaller parallelepipeds located underneath the structure. This allows these two support to rotate freely (the mesh conforms with those lines). The two smaller parallelepipeds at the top of the structure are loaded in a similar fashion, but with a downward prescribed motion of the action lines, with an amplitude that is proportional to $A(t)$, i.e. we reuse the loading function introduced in the previous example to simplify the presentation. The interface between the large beam and the four smaller parallelepipeds is represented by a unilateral frictionless contact model. We finally introduce two fibres as represented in Figure 10, the interface between the fibres and the matrix being modelled by the friction-type model derived previously.

The object composed of the 5 parallelepipeds is meshed conformingly to its boundary. The fibres are not meshed by the meshing software. Instead, they are introduced in a non-conforming manner using the technique proposed in this paper. In a similar fashion, we handle the four unilateral contact conditions described above nonconformingly using the primal/dual LaTIn-CutFEM algorithm [12], i.e. the four contact interfaces do not conform with the facets of the mesh and are represented by the zero isoline of a finite element level-set function.

Numerical results. The displacement of the system at the end of the first loading phase is represented in Figure 10. The set of elements that are intersected by the fibres is also displayed. We see that the fibres and the band of elements they are embedded in follow the global deformation of the structure, as expected.

The system presented here will not behave like the 2D system presented in the previous section. When $A(t)$ becomes negative at time $t = 1.5$, the two parallelepipeds onto which the prescribed motion is applied move upward without adhering to the remainder of the structure (traction forces cannot be transmitted by the unilateral contact interfaces). The beam will stay at rest until $t = 2.7$, after which it will undergo bending deformations again as induced by the downward motion of the two parallelepipeds. This resting time will allow us to study residual stresses, i.e stresses that have developed due to inelastic phenomena (i.e. friction), and do not go back to zero once the structure is fully unloaded.

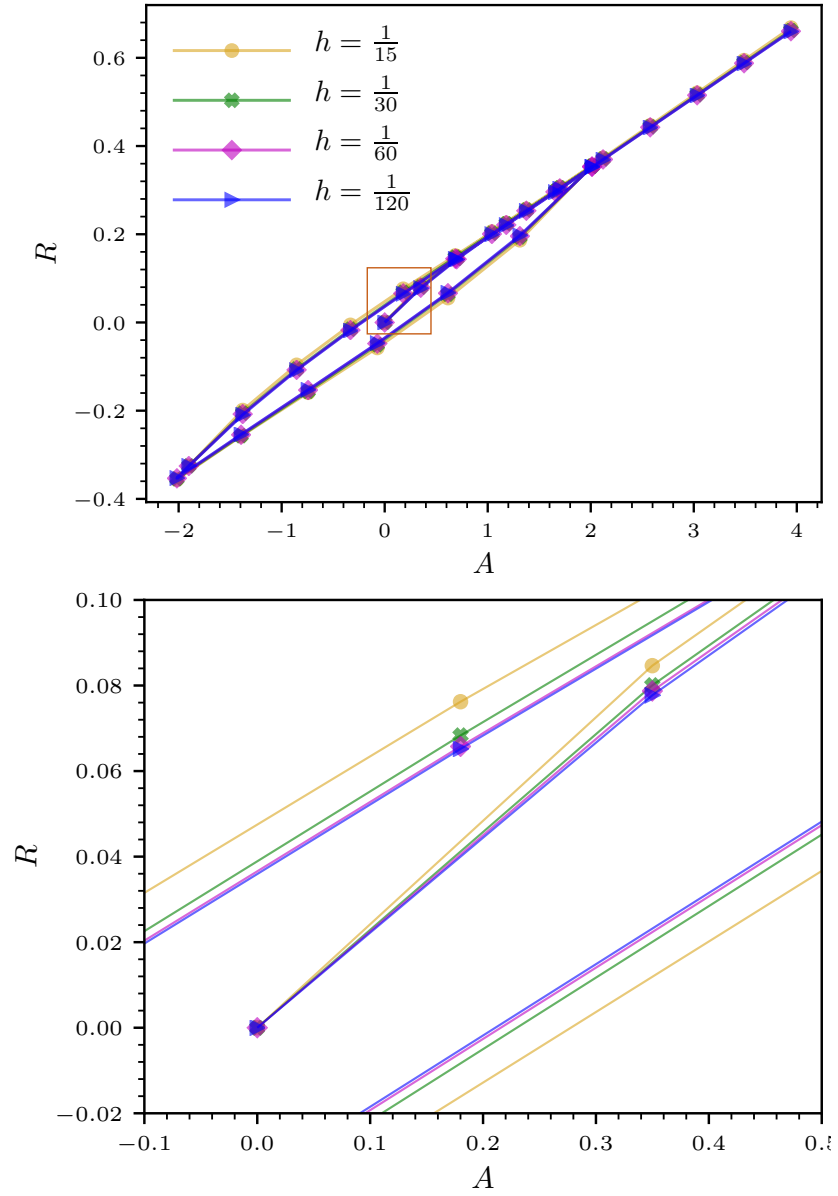


Figure 8: Global reaction force of the structure as a function of the prescribed extension. The hysteretic behaviour is due to the friction law. Convergence of this response curve can be seen when the mesh is progressively refined. The meshes used to produce these four curves are represented in Figure 7

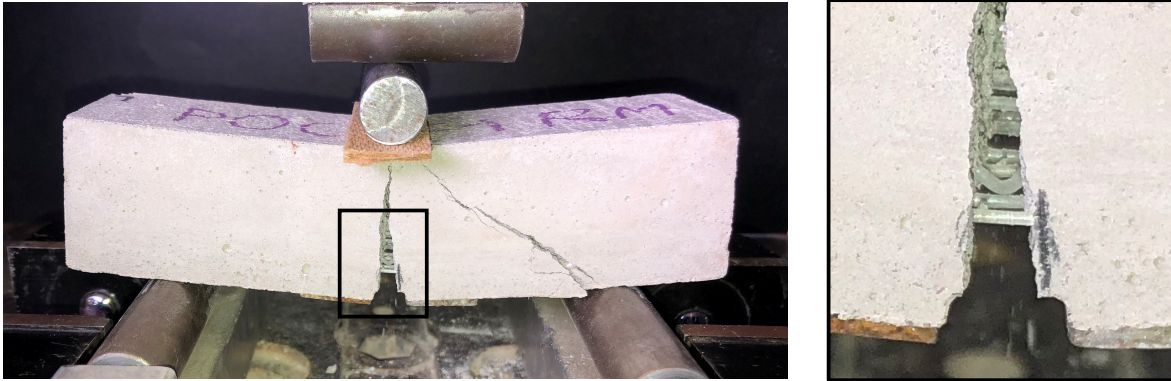


Figure 9: Notched concrete beam with embedded SMP fibres tested in flexure.

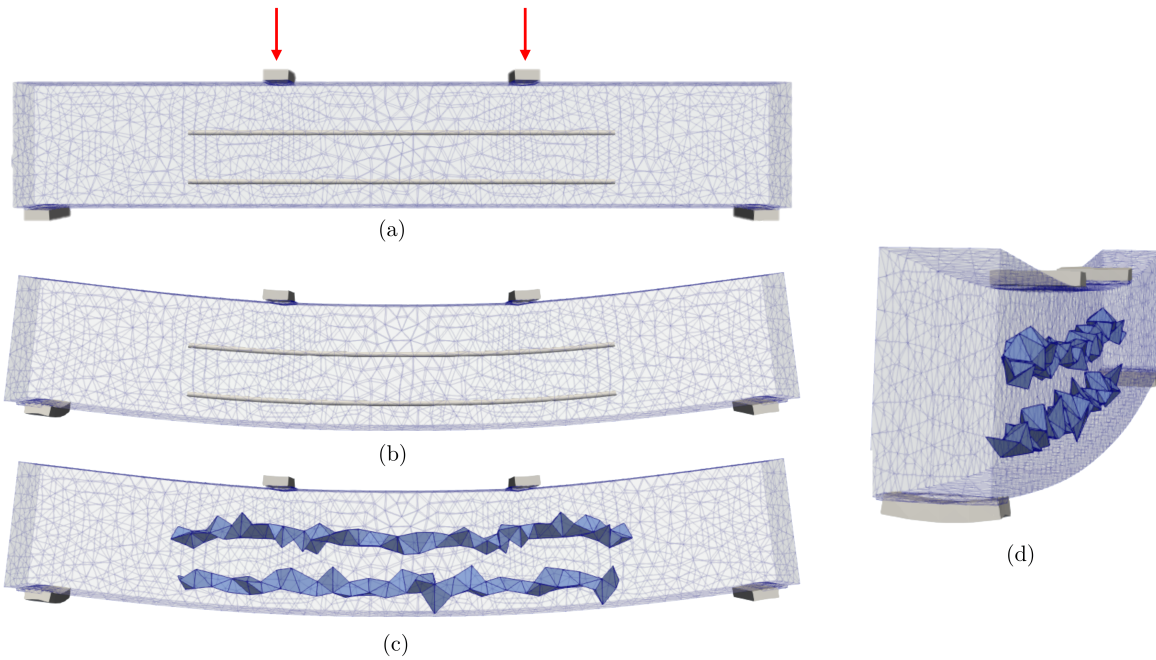


Figure 10: Beam structure undergoing four-point bending deformations. The two feet are fixed vertically, but their rotations in the plane of figure (a) are freely allowed. The two top parallelepipeds are vertically constrained to follow prescribed displacement $-A(t)$. They are also free to rotate. The embedded interface between the four smaller parallelepipeds and the large beam is unilateral frictionless contact. When $A(t)$ is negative, the top two smaller parallelepipeds loose contact with the beam, and the structure is at rest.

These residual stresses are shown in Figure 11. We see that when the structure is undergoing progressively increasing bending conditions, the bottom fibre is acting against the extension of the beam, while the top fibre acts against compression. During rest (subplot (b) in Figure 11), due to friction, these stress states do not subside completely, and a small amount of permanent bending deformations remains without external action.

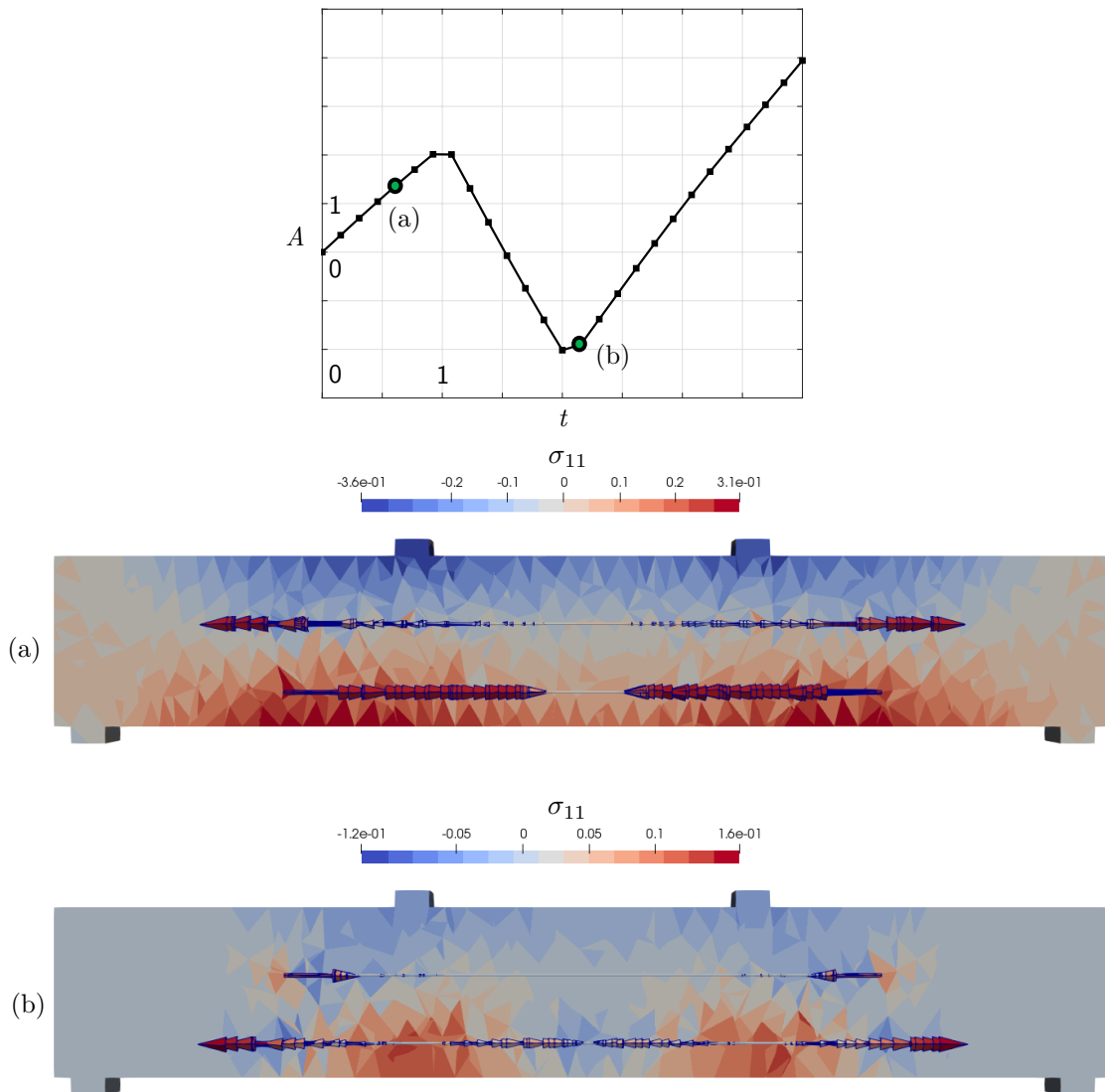


Figure 11: Lagrange multipliers of the fibre friction model: (a) development of fibre forces in reaction to bending deformations, limited in amplitude by plastic slip and (b) residual stresses at rest, once the two top parallelepipeds have lost contact with the beam strut. Stress σ_{11} is the longitudinal stress measured along the horizontal axis of the figure.

Effect of the numerical stabilisers. In Figure 12, we show the effect of the stabilisers introduced to make sure that the solution of finite element problems with nonconforming 1D embedded elastic elements is well-posed. The top picture is the representation of an uncontrolled deformation mode that appeared when setting ζ to a value that is very close to zero. The zero energy modes explode in amplitude. The restriction of the solution to the fibre is still correct, but carrying such large values of the degrees of freedom through long time analyses is of course not advisable. Setting ζ to a small but non-vanishing value, as suggested previously, ensures that such uncontrolled sets of degrees of freedom are eliminated from the system. This results in fully controlled deformations of bands of intersected elements, as shown in Figure 10 (last two subplots).

The same remarks can be made regarding Lagrange multiplier fields. When setting ζ_λ to a vanish-

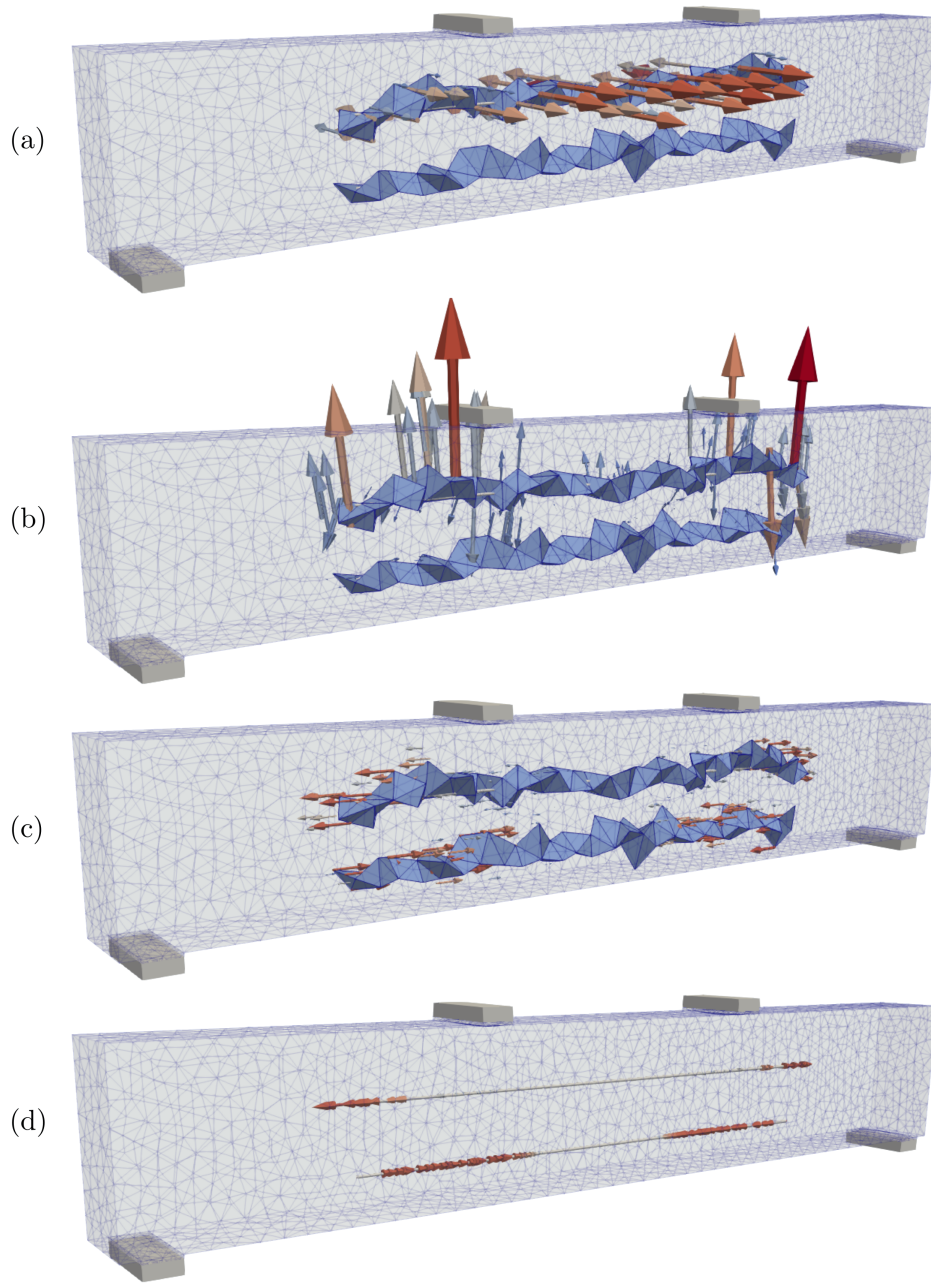


Figure 12: Effect of stabilisation terms on extended fibre fields: (a) uncontrolled extended displacement mode, (b) uncontrolled extended Lagrange multiplier modes, (c) regularised extended Lagrange multiplier and (d) restriction of the regularised extended Lagrange multiplier field to the 1D fibre domain.

ingly small value, uncontrolled modes develop, as seen in Figure 12 (a) and (b). A small regularisation parameter ensures that the problem is well-posed, which is exemplified by the beautiful purely axial distribution of the extended Lagrange multiplier field shown Figure 12 (c) and (d).

5.3 Fracture of quasi-brittle composites with randomly distributed short fibres

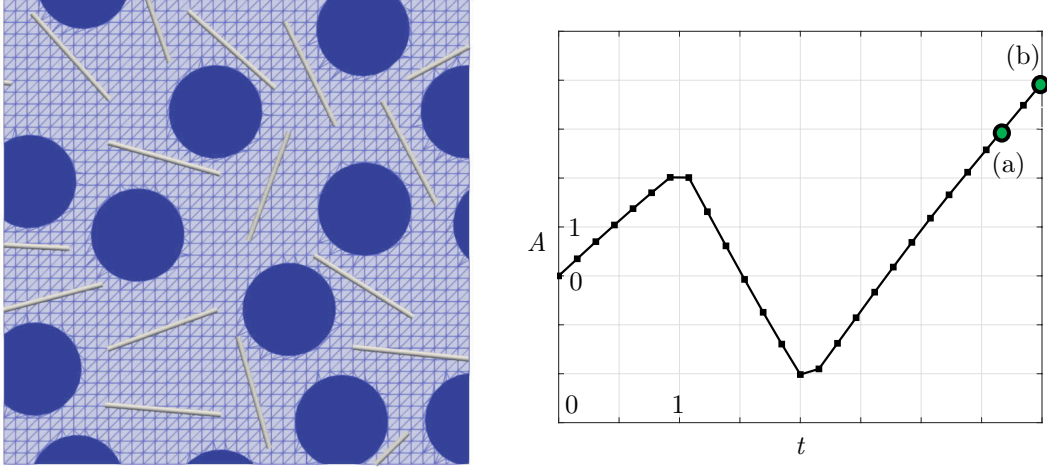


Figure 13: Geometry of the fracture mechanics model (left) and points of interest in the time analysis (right)

To further illustrate the capabilities of the proposed approach, we extend it to the simulation of damage in cement-based composite materials reinforced with randomly distributed short fibres. The overall mechanical behaviour as well as the crack propagation in these composites are largely governed by the crack-bridging action of fibres.

The problem setting is graphically described in Figure 13. The interface between fibres and matrix is now rigid (i.e. infinite friction coefficient Y). Uniform linear Dirichlet boundary conditions in the e_2 direction are now applied on the entire boundary $\partial\Omega$. We continue using function $A(t)$ to describe the overall evolution of the load with time. The perfect kinematic coupling between hard elastic inclusions and matrix is handled via the primal/dual LaTin-CutFEM algorithm. The new element in this example is the fact that the matrix can undergo elastic damage.

To represent damage, we use the staggered phase-field formulation presented in [25]. Bilinear form a_h is therefore modified as follows:

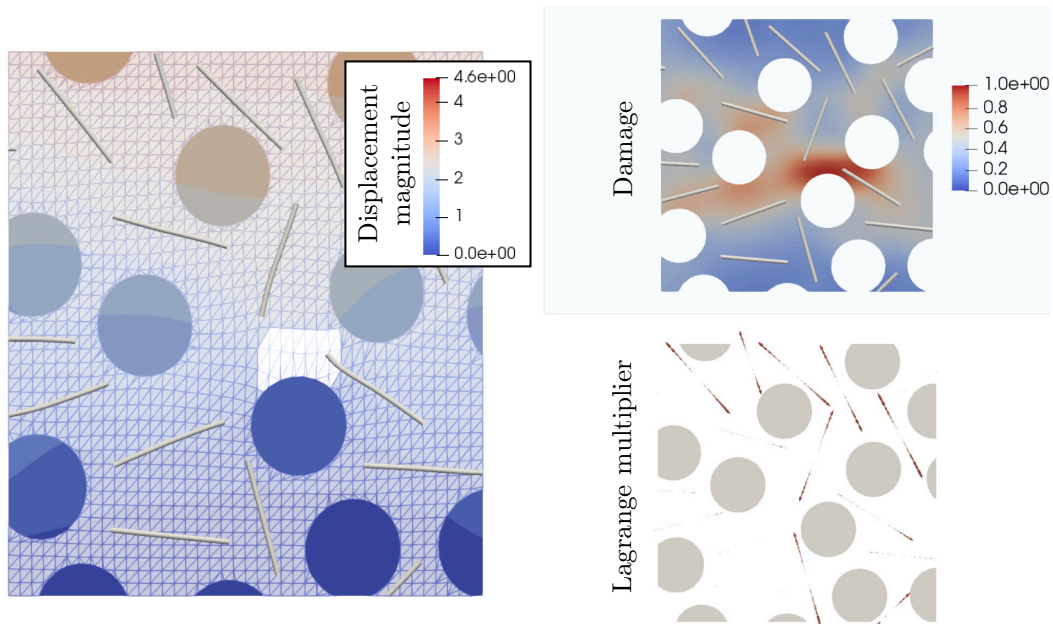
$$\begin{aligned}
 a_h((u_{m,h}, u_{f,h}), (\delta u_{m,h}, \delta u_{f,h})) &= \int_{\Omega} ((1 - d_h)^2 + \epsilon_d) \nabla_s u_{m,h} : C : \nabla_s \delta u_{m,h} dx \\
 &+ \int_{\Gamma_f} k_f \nabla_f u_{f,h} : \nabla_f \delta u_{f,h} dx \\
 &+ s_{\#,h}(u_{f,h}, \delta u_{f,h}).
 \end{aligned} \tag{48}$$

Field $\sigma_{m,h} := ((1 - d_h)^2 + \epsilon_d) C : \nabla_s \delta u_{m,h}$ is the Cauchy stress tensor and $d_h \in \mathcal{U}_h$ is a finite element field that represents damage. At the end of time step $t_n \in \mathcal{T}_{\Delta t}$, damage field d_h is updated by solving the following linear elliptic variational problem:

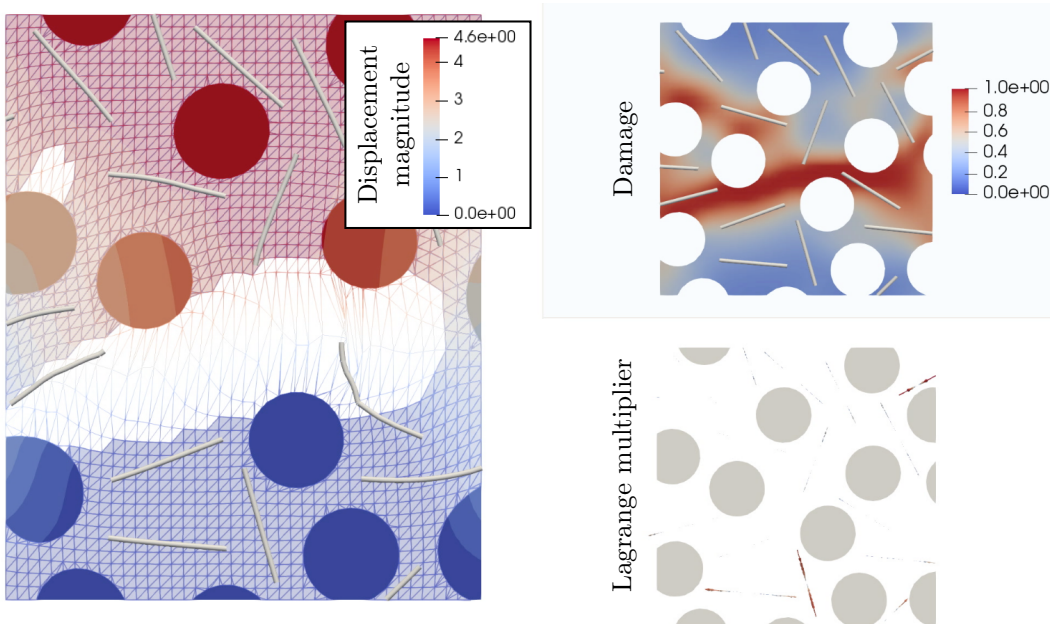
$$\forall \delta d_h \in \mathcal{U}_h, \quad \int_{\Omega} \left(1 + \frac{2l}{g_c} \mathcal{H}_h(x)\right) d_h \delta d_h dx + l^2 \int_{\Omega} \nabla d_h \cdot \nabla \delta d_h dx = \int_{\Omega} \frac{2l}{g_c} \mathcal{H}_h(x) \delta d_h dx. \tag{49}$$

In the above damage model, $\epsilon_d \ll 1$ is a small regularisation parameter, l is the length-scale of the phase-field model, which is set to 0.05 times the width of the computational domain, g_c is the energy release rate, and field \mathcal{H}_h is computed locally as follows, using the displacement obtained iteratively using the iterative LaTin solver described in this paper,

$$\forall x \in \Omega, \quad \mathcal{H}_h(x) = \max_{t \in \mathcal{T}_{\Delta t} | t \leq t_n} \left(\frac{1}{2} \nabla_s u_{m,h}|_x(t) : C : \nabla_s u_{m,h}|_x(t) \right). \tag{50}$$



(a)



(b)

Figure 14: Results obtained with the fracture mechanics model (phase-field) at two different analysis times: (a) crack initiation and (b) fully cracked computational model.

Our first results using the phase-field model together with the embedded fibre formulation are reported in Figure 14. The circular inclusions cannot be damaged, which can be formulated by setting g_c to a large value in the corresponding subdomain. In the left-hand-side plots of Figure 14, we do not represent elements that exhibit damage values exceeding 0.95, for visual purposes. The proposed algorithm remained stable throughout the analysis, yielding qualitatively sensible results. In particular, the stiff fibres prevent the crack from developing along directions that are orthogonal to their respective director vector. The Lagrange multipliers are well aligned with the fibres.

Further stability and convergence tests would be required to study the effect of the damage field on the overall stability of the unfitted finite element formulation. This is left to future investigations.

We note that a particular drawback of the proposed unfitted finite element approach is that fictitious domains corresponding to disconnected physical elements (i.e. two separate inclusions, two different fibres, a fibre and an inclusion), should not overlap for the numerical results to be sensible. This sets a lower bound on the element size, which may preclude their use in preliminary engineering studies where very coarse meshes are used to inexpensively study the overall behaviour of a complex system.

6 Conclusion

We have presented a stabilised cut finite element solver to simulate the micro-mechanics of fibre-reinforced composites. The fibre elements have their own degrees of freedom, allowing complex interface conditions and efficient iterative solvers to be devised. No specific mesh is required for the slender structural elements. The unidimensional mechanical fields are represented as 1D traces of background 2D or 3D finite element fields.

Starting from this elegant numerical strategy, we developed a primal-dual finite element formulation to simulate friction-restricted sliding between the fibres and the embedding material. We also designed an efficient LaTIn algorithm to solve the resulting stiff nonlinear system of equations.

Just like any CutFEM solver, ours needs to be stabilised to fully eliminate numerical instabilities resulting from arbitrary cutting and embedding of finite element meshes. To this end, we have proposed a natural combination of ghost-penalty regularisation to stabilise the projected gradient, and background mesh penalisation to eliminate uncontrolled gradients in the normal direction. This approach has also been used to stabilise the dual fields. We have shown that the method is stable, convergent, and versatile. It handles high levels of nonlinearities very well, which was shown in examples of featuring 1D/3D imperfect bonding and nonlinear damage mechanics.

This work is an important stepping stone towards the development of flexible virtual testing platforms, in particular for cement-based composite materials. Avenues for further research and developments are manifold. For instance, we would like to investigate how the proposed method can handle structural elements with bending energy, where locking is very likely to cause numerical issue. Similarly, the present investigations are limited to straight fibres, and an obvious extension would be to allow for curved fibres to be represented. Finally, we would like to be able to simulate pull-out, i.e. the reduction of added stiffness as fibres are progressively losing contact areas with embedding materials when cracks progressively open. This requires to move away from the assumption of small perturbation, and to continuously update the geometrical configuration of the embedded elements in the evolving embedding structure.

Declarations

Availability of data and materials. Not applicable

Competing interests. Not applicable

Funding. The authors gratefully acknowledge the financial support provided by the Welsh Government and Higher Education Funding Council for Wales through the Ser Cymru National Research Network in Advanced Engineering and Materials for Susanne Claus’ personal fellowship under grant NRNG06. All three authors have shared responsibility for maintaining the levels of enthusiasm and motivation that were required for this piece of work to be produced. The publishing fees of this article have been graciously covered by the French Association for Computational Mechanics (CSMA).

Authors’ contributions. The authors have jointly developed the proposed LaTIn-CutFEM framework for 1D-3D coupling. The authors have jointly designed and implemented the test cases. Pierre Kerfriden has written the manuscript.

Acknowledgements. Not applicable

References

- [1] Basava Raju Akula, Julien Vignollet, and Vladislav A. Yastrebov. MorteX method for contact along real and embedded surfaces: Coupling X-FEM with the Mortar method. *arXiv preprint arXiv:1902.04000*, 2019.
- [2] Pierre Alart and Alain Curnier. A mixed formulation for frictional contact problems prone to Newton like solution methods. *Computer methods in applied mechanics and engineering*, 92(3):353–375, 1991.
- [3] O. Allix, P. Kerfriden, and P. Gosselet. On the control of the load increments for a proper description of multiple delamination in a domain decomposition framework. *International Journal for Numerical Methods in Engineering*, 83:1518–1540, 2010.
- [4] Martin S. Alnæs, Jan Blechta, Johan Hake, August Johansson, Benjamin Kehlet, Anders Logg, Chris Richardson, Johannes Ring, Marie E. Rognes, and Garth N. Wells. The FEniCS project version 1.5. *Archive of Numerical Software*, 3(100):9–23, 2015.
- [5] Huu Phuoc Bui, Satyendra Tomar, and Stéphane PA Bordas. Corotational cut finite element method for real-time surgical simulation: Application to needle insertion simulation. *Computer Methods in Applied Mechanics and Engineering*, 345:183–211, 2019.
- [6] Erik Burman. Ghost penalty. *Comptes Rendus Mathématique*, 348(21-22):1217–1220, 2010.
- [7] Erik Burman, Susanne Claus, Peter Hansbo, Mats G. Larson, and André Massing. CutFEM: Discretizing geometry and partial differential equations. *International Journal for Numerical Methods in Engineering*, 104(7):472–501, 2015.
- [8] Erik Burman, Peter Hansbo, and Mats G. Larson. Augmented Lagrangian finite element methods for contact problems. *ESAIM: Mathematical Modelling and Numerical Analysis*, 53(1):173–195, 2019.
- [9] Erik Burman, Peter Hansbo, and Mats G. Larson. A simple finite element method for elliptic bulk problems with embedded surfaces. *Computational Geosciences*, 23(1):189–199, February 2019.
- [10] Erik Bürman, Peter Hansbo, Mats G. Larson, and André Massing. Cut finite element methods for partial differential equations on embedded manifolds of arbitrary codimensions. *ESAIM: Mathematical Modelling and Numerical Analysis*, 52(6):2247–2282, 2018.
- [11] Susanne Claus, Samuel Bigot, and Pierre Kerfriden. CutFEM Method for Stefan–Signorini Problems with Application in Pulsed Laser Ablation. *SIAM Journal on Scientific Computing*, 40(5):B1444–B1469, 2018.

- [12] Susanne Claus and Pierre Kerfriden. A stable and optimally convergent LaTIn-CutFEM algorithm for multiple unilateral contact problems. *International Journal for Numerical Methods in Engineering*, 113(6):938–966, 2018.
- [13] Susanne Claus and Pierre Kerfriden. A CutFEM method for two-phase flow problems. *Computer Methods in Applied Mechanics and Engineering*, 348:185–206, 2019.
- [14] Carlo D’Angelo and Anna Scotti. A mixed finite element method for Darcy flow in fractured porous media with non-matching grids*. *ESAIM: Mathematical Modelling and Numerical Analysis*, 46(2):465–489, 2012.
- [15] Frédéric Duboeuf and Eric Béchet. Embedded solids of any dimension in the X-FEM. Part I—Building a dedicated P1 function space. *Finite Elements in Analysis and Design*, 130:80–101, 2017.
- [16] Luca Formaggia, Alessio Fumagalli, Anna Scotti, and Paolo Ruffo. A reduced model for Darcy’s problem in networks of fractures*. *ESAIM: Mathematical Modelling and Numerical Analysis*, 48(4):1089–1116, 2014.
- [17] H. M. Gomes and A. M. Awruch. Some aspects on three-dimensional numerical modelling of reinforced concrete structures using the finite element method. *Advances in Engineering software*, 32(4):257–277, 2001.
- [18] Anita Hansbo and Peter Hansbo. A finite element method for the simulation of strong and weak discontinuities in solid mechanics. *Computer methods in applied mechanics and engineering*, 193(33-35):3523–3540, 2004.
- [19] M. Hirmand, M. Vahab, and A. R. Khoei. An augmented Lagrangian contact formulation for frictional discontinuities with the extended finite element method. *Finite Elements in Analysis and Design*, 107:28–43, 2015.
- [20] Anthony Jefferson, Christopher Joseph, Robert Lark, Ben Isaacs, Simon Dunn, and Brendon Weager. A new system for crack closure of cementitious materials using shrinkable polymers. *Cement and Concrete Research*, 40(5):795–801, 2010.
- [21] P. Kerfriden, O. Allix, and P. Gosselet. A three-scale domain decomposition method for the 3D analysis of debonding in laminates. *Computational Mechanics*, 44(3):343–362, 2009.
- [22] P. Ladevèze, A. Nouy, and O. Loiseau. A multiscale computational approach for contact problems. *Computer Methods in Applied Mechanics and Engineering*, 191:4869–4891, 2002.
- [23] Benoît Lé, Grégory Legrain, and Nicolas Moës. Mixed dimensional modeling of reinforced structures. *Finite Elements in Analysis and Design*, 128:1–18, 2017.
- [24] R Maddalena, L Bonanno, B Balzano, J Sweeney, and I Mihai. A crack closure system for cementitious composite materials using knotted shape memory polymer (k-SMP) fibres. *Cement & Concrete Composites*, Under review, 2019.
- [25] Christian Miehe, Fabian Welschinger, and Martina Hofacker. Thermodynamically consistent phase-field models of fracture: Variational principles and multi-field FE implementations. *International Journal for Numerical Methods in Engineering*, 83(10):1273–1311, 2010.
- [26] José Manuel Navarro-Jiménez, Manuel Tur, José Albelda, and Juan José Ródenas. Large deformation frictional contact analysis with immersed boundary method. *Computational Mechanics*, pages 1–18, 2018.

- [27] Machhour Sadek and Isam Shahrouh. A three dimensional embedded beam element for reinforced geomaterials. *International journal for numerical and analytical methods in geomechanics*, 28(9):931–946, 2004.
- [28] Mubbada Suidan and William C. Schnobrich. Finite element analysis of reinforced concrete. *Journal of the structural division*, 99(st1), 1973.

A Unregularised LaTIn local stage

By manipulating the ascent search direction, we can easily show that

$$2\tilde{F}_{m,h}^{k+\frac{1}{2}} - (F_{m,h}^k - F_{f,h}^k) - \gamma \left((\tilde{W}_{m,h}^{k+\frac{1}{2}} - \Delta\tilde{W}_{f,h}^{k+\frac{1}{2}}) - (\Delta W_{m,h}^k - \Delta W_{f,h}^k) \right) = 0, \quad (51)$$

where the Δ symbol denotes a time increment, e.g. $\Delta\tilde{W}_{m,h}^{k+\frac{1}{2}} := \tilde{W}_{m,h}^{k+\frac{1}{2}} - \tilde{W}_{m,h}^*$. The previous expression implicitly assumes that the LaTIn solver used to solve the incremental problem arising at time t_n has converged.

Normal problem. The previous equation can be projected orthogonally to the fibres director vector. Using the fact that $\Pi_f^\perp \left(\Delta\tilde{W}_{m,h}^{k+\frac{1}{2}} - \Delta\tilde{W}_{f,h}^{k+\frac{1}{2}} \right) = 0$, which is a direct contextualisation of (32), we obtain the expression of $\Pi_f^\perp \tilde{F}_{m,h}^{k+\frac{1}{2}}$ by solving

$$\Pi_f^\perp \left(2\tilde{F}_{m,h}^{k+\frac{1}{2}} - (F_{m,h}^k - F_{f,h}^k) - \gamma \left(-(\Delta W_{m,h}^k - \Delta W_{f,h}^k) \right) \right) = 0. \quad (52)$$

Tangential problem. We now solve the equations of plasticity in the direction of the fibres director vector. We proceed by trial and testing, hypothesising that $\left(\Delta\tilde{W}_{m,h}^{k+\frac{1}{2}} - \Delta\tilde{W}_{f,h}^{k+\frac{1}{2}} \right) \cdot t_f = 0$, which means that there is no sliding between matrix and fibre phases. If this assumption was true, we would have that

$$\left(2\tilde{F}_{m,h}^{k+\frac{1}{2}} - (F_{m,h}^k - F_{f,h}^k) - \gamma \left(-(\Delta W_{m,h}^k - \Delta W_{f,h}^k) \right) \right) \cdot t_f = 0, \quad (53)$$

We can now check whether the previously made hypothesis is consistent with equation $f_f \left(\tilde{F}_{m,h}^{k+\frac{1}{2}} \right) \leq 0$. If it is the case, we can safely return

$$\tilde{F}_{m,h}^{k+\frac{1}{2}} = \left(\tilde{F}_{m,h}^{k+\frac{1}{2}} \cdot t_f \right) t_f + \Pi_f^\perp \tilde{F}_{m,h}^{k+\frac{1}{2}} \quad (54)$$

and proceed to the smoothing step of the local stage. Otherwise, our hypothesis is not true: there is sliding, which means that necessarily,

$$\tilde{F}_{m,h}^{k+\frac{1}{2}} \cdot t_f = -Y \operatorname{sign} \left((\Delta\tilde{W}_{m,h}^k - \Delta\tilde{W}_{f,h}^k) \cdot t_f \right). \quad (55)$$

We now make the hypothesis that the sign of the relative velocity between fibre and matrix is positive. In this case, we have that

$$t_f \cdot \left(-2Y - (F_{m,h}^k - F_{f,h}^k) - \gamma \left((\Delta\tilde{W}_{m,h}^{k+\frac{1}{2}} - \Delta\tilde{W}_{f,h}^{k+\frac{1}{2}}) - (\Delta W_{m,h}^k - \Delta W_{f,h}^k) \right) \right) = 0, \quad (56)$$

from which we can compute $\left[t_f \cdot \Delta\tilde{W}_h^{k+\frac{1}{2}} \right] = t_f \cdot \left(\Delta\tilde{W}_{m,h}^{k+\frac{1}{2}} - \Delta\tilde{W}_{f,h}^{k+\frac{1}{2}} \right)$. If the sign of this quantity is positive, we return

$$\tilde{F}_{m,h}^{k+\frac{1}{2}} = -Y t_f + \Pi_f^\perp \tilde{F}_{m,h}^{k+\frac{1}{2}}. \quad (57)$$

Otherwise, we return

$$\tilde{F}_{m,h}^{k+\frac{1}{2}} = Y t_f + \Pi_f^\perp \tilde{F}_{m,h}^{k+\frac{1}{2}}. \quad (58)$$